Rydberg electromagnetically induced transparency and absorption of strontium triplet states in a weak microwave field

Yan-Li Zhou [1,*] Dong Yan [2] and Weibin Li [3,†]

[1]*Department of Physics, College of Liberal Arts and Sciences, and Interdisciplinary Center for Quantum Information, National University of Defense Technology, Changsha 410073, China*

[2]*School of Science and Key Laboratory of Materials Design and Quantum Simulation, Changchun University, Changchun 130022, China*

[3]*School of Physics and Astronomy, and Centre for the Mathematics and Theoretical Physics of Quantum Non-equilibrium Systems, University of Nottingham, Nottingham NG7 2RD, United Kingdom*

(Received 29 January 2022; accepted 9 May 2022; published 19 May 2022)

We study theoretically laser excitation of Rydberg triplet states of strontium atoms in the presence of weak microwave (MW) fields. Starting from the ground state $5s^2\,{}^1S_0$, the Rydberg excitation is realized through the metastable, triplet $5s5p^3P_1$ state, whose decay rate γ_2 is $2\pi \times 7.5$ kHz, much smaller than the one in the singlet state or alkali-metal atoms. The influences of γ_2 on the transparency and absorption spectrum in the electromagnetically induced transparency (EIT), and electromagnetically induced absorption (EIA) regime are examined. Narrow transparent windows (EIT) or absorption peaks (EIA) are found, whose distance in the spectrum depends on the Rabi frequency of the weak MW field. It is found that the spectrum exhibits higher contrast than using the singlet state or alkali-metal atoms in typical situations. Using the metastable intermediate state, we find that the resonance fluorescence of Sr gases exhibits very narrow peaks, which are modulated by the MW field. When the MW field is weaker than the probe and control light, the spectrum distance of these peaks is linearly proportional to Ω_m. This allows us to propose an alternative way to sense very weak MW fields through resonance fluorescence. Our study shows that the Sr triplet state could be used to develop the Rydberg MW electrometry that gains unique advantages.

DOI: 10.1103/PhysRevA.105.053714

I. INTRODUCTION

Using their large electric-dipole moments and many dipole allowed transitions, Rydberg atoms are utilized to sense weak electromagnetic fields from the microwave (MW) to terahertz frequency range [1–4]. These sensing applications are largely based on alkali-metal atoms, such as Cs [5–7] and Rb [4,8]. Commonly, atoms are laser excited to a low-lying, intermediate state, and then to a Rydberg state by a control light. A MW field couples the Rydberg state near resonantly to a different Rydberg state. Both Rydberg states have long lifetime (10–100 μs typically), while the linewidth of the intermediate state is large [9–11] (e.g., about $2\pi \times 6.07$ MHz in the $5p$ state of Rb and $2\pi \times 5.22$ MHz in the $6p$ state of Cs). To sensitively probe the electric component of MW fields, one typically relies on two quantum interference phenomena, i.e., electromagnetically induced transparency (EIT) and the Autler-Townes (AT) effects [4,7,12,13]. Here the Rydberg-MW field coupling gives rise to two Rydberg dressed states, which generate two transparent windows (the AT splitting). The distance of the AT splitting is determined by the Rabi frequency of the MW electric field, which serves as the basis in the Rydberg atom based MW electrometry. This method is influenced by various parameters, such as the control laser strength and decay rate in the intermediate state. In particular, the large decay rate affects the lowest MW field that can be sensed [14]. A different method, based on the electromagnetically induced absorption (EIA) [15], has been demonstrated experimentally [14]. In the EIA method, the intermediate state is adiabatically eliminated through large single-photon detuning. The MW coupled AT states lead to two absorption maxima, whose distance equals the MW Rabi frequency when the latter is much larger than the ac Stark shift. This approach largely avoids impacts from the intermediate state, and can sense weak MW fields as low as 100 μV/cm [14]. However, the visibility of the absorption spectrum is suppressed because the overall absorption is much weaker.

In recent years, Rydberg states of alkaline-earth-metal atoms have attracted growing interest [16,17]. Experiments have observed the Rydberg state excitation [9], blockade effects [18,19], Rydberg dressing [20], and Rydberg polaron [21] in gases of strontium atoms. Compared to alkali-metal atoms, one of the key differences is that Rydberg states can be excited through intermediate, triplet states. For example, the linewidth of the triplet $5s5p^3P_1$ state of Sr atoms is $\gamma_2 = 2\pi \times 7.5$ kHz. The long coherence time in the triplet state plays important roles in the study of Rydberg physics of alkaline-earth-metal atoms when excited through EIT [16], such as quantum clock networks [22], spin squeezing [23] via Rydberg dressed interactions [24,25], and Rydberg atom based high-precision quantum metrology [23,26,27]. When developing MW sensing with alkaline-earth atoms, the em-

*ylzhou@nudt.edu.cn
†weibin.li@nottingham.ac.uk

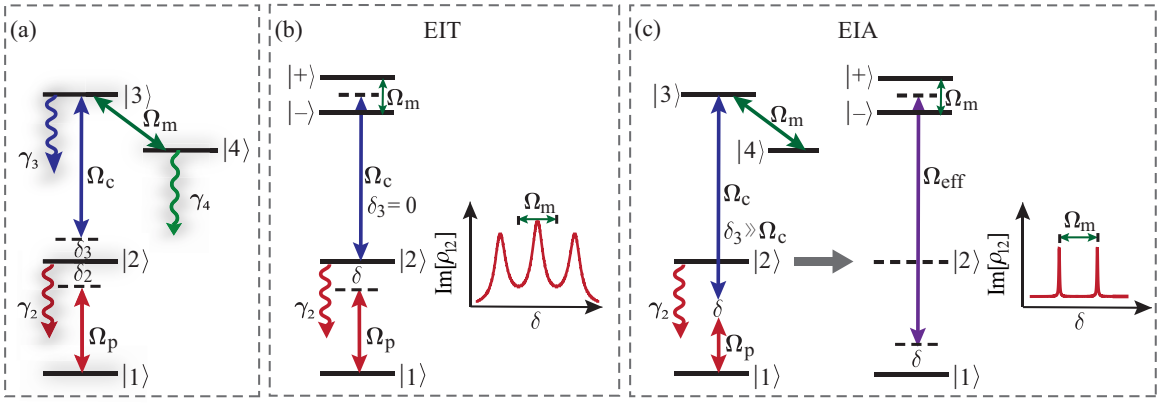

FIG. 1. (a) Level scheme. A probe laser (Rabi frequency Ω_p and detuning δ_2) and a control laser (Rabi frequency Ω_c and detuning δ_3) couple the transitions between state $|1\rangle \to |2\rangle$ and $|2\rangle \to |3\rangle$, respectively. A near-resonant MW field couples Rydberg states $|3\rangle \to |4\rangle$ with Rabi frequency Ω_m. (b) EIT and AT effect. When the control laser is resonant $\delta_3 = 0$, the resonant MW field splits the EIT transmission maximum into two peaks. The distance of the two peaks, i.e., the AT splitting of the dressed states $|+\rangle$ and $|-\rangle$, is approximately equal to Ω_m. (c) EIA scheme is achieved when both the control and probe light are far detuned, while two-photon resonance is approximately maintained. The MW field induces two absorption peaks with splitting Ω_m near the two-photon resonant transition.

ployment of the singlet or triplet intermediate state will have different optical responses [28,29]. Therefore, it is interesting to understand the roles played by the triplet state in EIT as well as in developing MW electrometry with Sr atoms.

In this work, we study the AT effect of Sr atoms when Rydberg states are coupled by a MW field. The Rydberg state is laser excited via the triplet $5s5p\,^3P_1$ state. We focus on influences of the weak decay rate in the metastable state. In the stationary EIT spectrum of Sr atoms, transparent windows are surrounded by strong absorption peaks, leading to high contrast signals even when both the MW and probe field Rabi frequency are of the same order of magnitude of the triplet decay rate γ_2. Under the large one-photon detuning condition, the distance between EIA peaks can be used to determine the MW Rabi frequency [14]. We show that high contrast can be realized through EIA when both the MW and probe field are close to γ_2.

Furthermore, we propose an alternative way to sense the MW field based on resonance fluorescence [30]. Resonance fluorescence is widely used in optical and atomic physics [31]. Different from the EIT and EIA method, photons randomly scattered by atoms are measured in resonance fluorescence. We show that the narrow linewidth of Sr atoms leads to well-separated fluorescence peaks. We identify the linear regime where the distance of the peaks is proportional to the MW Rabi frequency. Moreover, the time-dependent resonance fluorescence is employed to capture the slow timescale in the optical response, determined by γ_2. Here we show that resonance fluorescence can be used to sense MW fields with Rydberg states of Sr atoms.

The remainder of the paper is organized as follows. In Sec. II, we present the system whose dynamics is modeled by a quantum master equation of four-level atoms. In Sec. III, optical responses of the system in the presence of MW fields are discussed. We show the spectrum of the optical response in both the EIT and EIA regimes. A comparison between Rb and Sr atoms shows that high contrast optical responses can be obtained in Sr atoms. In Sec. IV, we investigate the roles of the intermediate state played in the dynamics and resonance fluorescence. It is found that resonance fluorescence can also be used to quantify the MW field. The main results and conclusions of this work are summarized in Sec. V.

II. SYSTEM AND MODEL

The laser-MW-coupled atom is described by a four-level model, as depicted in Fig. 1(a). The probe light of frequency ω_p drives the transition from the atomic ground state $|1\rangle$ to an intermediate state $|2\rangle$ with Rabi frequency Ω_p and detuning $\delta_2 = \omega_{21} - \omega_p$. A strong control light of frequency ω_c acts on the transition between state $|2\rangle$ and Rydberg state $|3\rangle$ with Rabi frequency Ω_c and detuning $\delta_3 = \omega_{32} - \omega_c$. The MW field with frequency ω_m couples two Rydberg states $|3\rangle$ and $|4\rangle$ with Rabi frequency Ω_m and detuning $\delta_m = \omega_{43} - \omega_m$. γ_i denotes the decay rate from state $|i\rangle$ to $|1\rangle$. In the electric dipole and rotating-wave approximation, the Hamiltonian of the system is given by ($\hbar \equiv 1$) [14]

$$H = H_d + \tfrac{1}{2}[\Omega_p\sigma_{12} + \Omega_c\sigma_{23} + \Omega_m\sigma_{34} + \text{H.c.}], \qquad (1)$$

where $\sigma_{ab} = |a\rangle\langle b|$ (a, b =1, 2, 3, and 4), and $H_d = \delta_2\sigma_{22} + \delta\sigma_{33} + \delta_4\sigma_{44}$ with $\delta = \delta_2 + \delta_3$ and $\delta_4 = \delta_2 + \delta_3 + \delta_m$. The two-photon detuning takes into account the single-photon probe field detuning δ_2 and control field detuning δ_3. Due to spontaneous decays in the intermediate state and Rydberg states, the dynamics of the density matrix ρ is governed by a quantum master equation,

$$\frac{d}{dt}\rho = \mathcal{L}\rho = -i[H, \rho] + \sum_{i=2}^{4}\gamma_i L(\sigma_{1i})\rho, \qquad (2)$$

with the Liouville $\mathcal{L}$ and dissipator $L(\cdot)\rho = (\cdot)\rho(\cdot)^\dagger - \{(\cdot)^\dagger(\cdot), \rho\}/2$, and the jump operator is given by $\sigma_{1j} = |1\rangle\langle i|$. Here we assume that Rydberg states directly decay to the ground state $|1\rangle$, while neglecting cascade decay to multiple low-lying electronic states. The dephasing of various electronic states has been neglected.

Focusing on Rydberg triplet states of Sr atoms, we consider the ground state $|1\rangle = |5s^2\,^1S_0\rangle$ and intermediate state

$|2\rangle = |5s5p\,^3P_1\rangle$. State $|2\rangle$ couples to a Rydberg state $|3\rangle = |5sns\,^3S_1\rangle$ [18,19], or $|5snd\,^3D_1\rangle$ [10]. A MW field couples state $|3\rangle$ to a neighboring Rydberg state $|4\rangle = |5sn'p\,^3P_1\rangle$. Depending on the principal quantum numbers, lifetimes in Rydberg states typically range from a few to tens of microseconds [32], leading to decay rates $\gamma_{3,4} \sim 2\pi \times 1 \ldots 100$ kHz. In the following, we will compare the optical response of Sr triplet states with conventional situations, where the decay rate of the intermediate state is large. The latter can be realized, for example, by using the Sr singlet state or alkali-metal atoms. To be concrete, the $5S_{1/2}(F=3) \to 5P_{3/2}(F=4) \to 50D_{5/2} \to 51P_{3/2}$ transition of ^{85}Rb atoms will be considered as an example, where $\gamma_2 \approx 2\pi \times 6$ MHz [33]. While the Rydberg decay rate is similar in both cases, the order of magnitude difference of the decay rate in the intermediate states leads to very different optical responses, as will be illustrated in the following.

III. MW MODULATED EIT AND EIA

The transmission of the probe light is $I_f = I_0 \exp(-\alpha L)$, where L and α are the length of the medium and absorption coefficient. The absorption coefficient $\alpha \propto \mathrm{Im}(\rho_{12})$ [34]. Hence our analysis will be focusing on ρ_{12}. First, the steady state of the master equation can be solved perturbatively [34]. In the limit of the weak probe light and with the initial state $\rho(0) = |1\rangle\langle 1|$, the master equation in the linear order of Ω_p is approximately given by

$$\dot{\rho_{12}} \simeq \left(i\delta_2 - \frac{\gamma_2}{2}\right)\rho_{12} + i\frac{\Omega_c}{2}\rho_{13} + i\frac{\Omega_p}{2}, \tag{3}$$

$$\dot{\rho_{13}} \simeq \left(i\delta - \frac{\gamma_3}{2}\right)\rho_{13} + i\frac{\Omega_c}{2}\rho_{12} + i\frac{\Omega_m}{2}\rho_{14}, \tag{4}$$

$$\dot{\rho_{14}} \simeq \left(i\delta_4 - \frac{\gamma_4}{2}\right)\rho_{14} + i\frac{\Omega_m}{2}\rho_{13}. \tag{5}$$

The analytic expression of the coherence between states $|1\rangle$ and $|2\rangle$ in the steady state is [33,35]

$$\rho_{12} \approx i\frac{|\Omega_m|^2 + \Gamma_3\Gamma_4}{\Gamma_2|\Omega_m|^2 + \Gamma_4|\Omega_c|^2 + \Gamma_2\Gamma_3\Gamma_4}\Omega_p, \tag{6}$$

where $\Gamma_2 = \gamma_2 - 2i\delta_2$, $\Gamma_3 = \gamma_3 - 2i\delta$, and $\Gamma_4 = \gamma_4 - 2i\delta_4$. The absorption of the probe light is determined by the imaginary part of ρ_{12}, while the real part gives the dispersion. Here a crucial approximation in deriving the steady solution is that Ω_p is assumed to be small. We note that such perturbative approach is valid in the case of alkali-metal atoms (e.g., Rb) where the condition $\gamma_2 \gg \Omega_2$ can be met. In the case of Sr triplet states, we will examine the validity of the perturbative result by comparing the perturbative and numerical calculations.

In the EIT regime, both the control light and MW field are resonant with respect to the underlying transition, i.e., $\delta_3 = \delta_m = 0$. The MW field causes the AT splitting, whose distance depends on the MW Rabi frequency. This relation can be used to accurately sense the properties of MW fields [4]. Recently, Liao *et al.* [14] have experimentally studied EIA of Rb atoms. Their experiment shows that Ω_m can be determined through measuring the absorption spectrum. EIA of Sr atoms has not been studied thoroughly, which will be examined in the following.

A. EIT regime

In the case of alkali-metal atoms, decay in Rydberg states is typically not important, as typically $\gamma_3 \sim \gamma_4 \ll \gamma_2$. When the coupling and MW field are resonant with respect to the transitions, i.e., $\delta_3 = \delta_m = 0$, the coherence is reduced to

$$\rho_{12} \approx -\frac{4\delta^2 - \Omega_m^2}{2\delta\left(4\delta^2 - \Omega_c^2 - \Omega_m^2\right) + i\gamma_2\left(4\delta^2 - \Omega_m^2\right)}\Omega_p. \tag{7}$$

Both the imaginary and real parts of the coherence vanish when $\delta = \pm\Omega_m/2$, leading to two transparent windows. When $\delta = 0$, or $\delta = \pm\sqrt{\Omega_c^2 + \Omega_m^2}/2$, the coherence becomes a pure imaginary number, $\rho_{12} = -i\Omega_p/\gamma_2$. This leads to strong absorption, whose peak increases with smaller γ_2. Moreover, the coherence is pure imaginary when all the fields are resonant,

$$\rho_{12} = i\frac{\gamma_3\gamma_4 + \Omega_m^2}{\gamma_4\Omega_c^2 + \gamma_2\left(\gamma_3\gamma_4 + \Omega_m^2\right)}\Omega_p. \tag{8}$$

We define the saturation of the absorption with $s = |\rho_{12}|^2$. With $\gamma_2 \gg \gamma_3, \gamma_4$, the saturation is approximately given by

$$s \approx s_0 = \frac{\Omega_p^2}{\gamma_2^2}, \tag{9}$$

which indicates the saturation is small in conventional EIT when $\gamma_2 \gg \Omega_p$.

To verify the perturbation analysis, we show numerical results in Figs. 2(a)–2(d) obtained by solving the master equation (2). Transparent windows are found at $\delta = \pm\Omega_m/2$, denoted by the open circles in Figs. 2(a)–2(c), which agree with the numerical result. Two absorption peaks are visible at $\delta = \pm\sqrt{\Omega_m^2 + \Omega_c^2}/2$, and a weak absorption line appears at $\delta = 0$, whose height is determined by s_0. This absorption line becomes stronger when increasing Ω_m. In Fig. 2(d), we plot the resonant absorption at $\delta = 0$. When Ω_p is much smaller than γ_2, the saturation s is quadratic with Ω_p; see Eq. (9). When Ω_p is large, the perturbation theory cannot predict the absorption accurately.

The above analysis shows that care must be taken when considering Sr atoms, where one typically encounters $\gamma_2 < \Omega_p$. Moreover, as Rydberg state decay rates γ_3 and γ_4 are comparable with the respective γ_2, according to Eq. (6) one can get $\mathrm{Im}[\rho_{12}] \propto \gamma_3\gamma_4$ at the transparent windows centered at $\delta = \pm\Omega_m/2$. It means that the minima of $\mathrm{Im}[\rho_{12}]$ do not reach zero with nonzero γ_3 and γ_4 [see Figs. 2(e)–2(g)]. Therefore, the probe light will experience losses, regardless of the detuning, and this could reduce the visibility of the transmission spectrum.

With nonzero γ_3 and γ_4, the saturation at resonance becomes

$$s_1 \approx \left[\frac{\left(\gamma_3^2 + \Omega_m^2\right)\Omega_p}{\gamma_2\left(\Omega_m^2 + \gamma_3^2\right) + \gamma_3\Omega_c^2}\right]^2, \tag{10}$$

where we have assumed $\gamma_3 = \gamma_4$. Equation (10) indicates that the saturation will be affected by the finite Rydberg state decay rates $\gamma_{3(4)}$, Ω_p, and Ω_m, even when $\Omega_p \ll \gamma_2$ [see Fig. 2(h)]. In addition to the absorption peak at resonance,

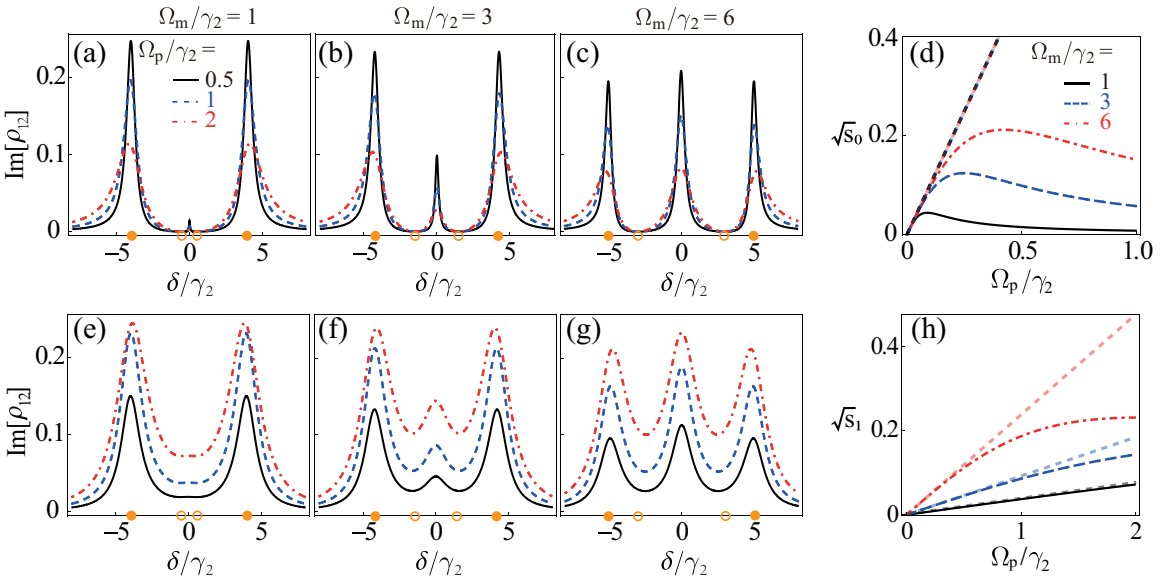

FIG. 2. (a)–(c) Imaginary parts of the coherence $\mathrm{Im}[\rho_{12}]$ by varying the two-photon detuning for (a) $\Omega_m = \gamma_2$, (b) $\Omega_m = 3\gamma_2$, and (c) $\Omega_m = 6\gamma_2$ when $\gamma_3 = \gamma_4 = 0$. In each panel, the solid, dashed, and dot-dashed curves correspond to $\Omega_p = 0.5\gamma_2$, γ_2, and $2\gamma_2$. The open circle and filled circle in the axis give the minimal and maximal locations of $\mathrm{Im}[\rho_{12}]$ at $\delta = \pm\Omega_m/2$ and $\delta = \pm\sqrt{\Omega_m^2 + \Omega_c^2}/2$, respectively. The numerical data agree with the perturbative calculations excellently. (d) $\sqrt{s_0}$ when $\gamma_3 = \gamma_4 = \delta_2 = 0$. The other parameters are $\delta_3 = \delta_m = 0$, and $\Omega_c = 8\gamma_2$. The solid, dashed, and dot-dashed curves correspond to $\Omega_m = \gamma_2, 3\gamma_2$, and $6\gamma_2$. The dotted curves are the analytical results shown in Eq. (9). (e)–(g) $\mathrm{Im}[\rho_{12}]$ for (e) $\Omega_m = \gamma_2$, (f) $\Omega_m = 3\gamma_2$, and (g) $\Omega_m = 6\gamma_2$ when $\gamma_3 = \gamma_4 = 2\gamma_2$. (h) $\sqrt{s_1}$ when $\gamma_3 = \gamma_4 = 2\gamma_2$. The solid, dashed, and dot-dashed curves correspond to $\Omega_m = \gamma_2, 3\gamma_2$, and $6\gamma_2$, while the dotted curves are the analytical results shown in Eq. (10).

two more absorption peaks are found at $\delta \approx \pm\sqrt{\Omega_c^2 + \Omega_m^2}/2$, which can be seen in Figs. 2(e)–2(g).

The distance between the AT splitting is independent of γ_2 and Ω_p, as shown in Figs. 3(a) and 3(b). A notable change is that the absorption becomes stronger and its linewidth becomes smaller when decreasing γ_2. When fixing γ_2, larger Ω_p will decrease the absorption and increase linewidth. Here the contrast between the smallest and largest $\mathrm{Im}[\rho_{12}]$ becomes smaller when Ω_p or γ_2 increases. To capture such contrast, we define visibility $V = (R_{\max} - R_{\min})/(R_{\max} + R_{\min})$, where $R_{\min}$ and $R_{\max}$ are the minimum and maximal value of $\mathrm{Im}[\rho_{12}]$. Large visibility means it would be easier to observe the nonuniform profile of the spectrum and provide strong signals. As shown in Figs. 3(c) and 3(d), the visibility will decrease due to the sharp decrease of maximum absorption coefficients as γ_2 and Ω_p increase. A potential drawback is that smaller γ_2 leads to slightly wider transparent windows at the AT splitting [Fig. 3(a)].

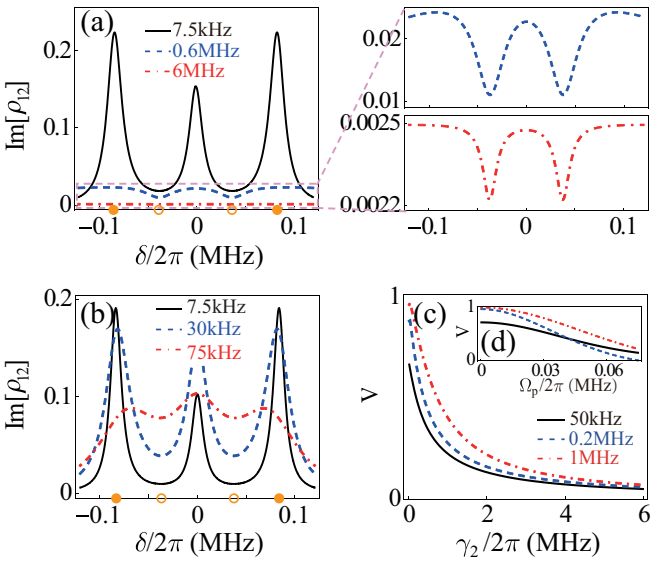

FIG. 3. (a) $\mathrm{Im}[\rho_{12}]$ with $\gamma_2/2\pi = 7.5$ kHz (black solid line), 0.6 MHz (blue dashed line), and 6 MHz (red dot-dashed line). The other parameters are $\delta_3 = \delta_m = 0$, $\gamma_3/2\pi = \gamma_4/2\pi = 15$ kHz, $\Omega_p = \gamma_3$, $\Omega_c = 10\gamma_3$, and $\Omega_m = 5\gamma_3$. The open circle and filled circle in the axis give the minimal and maximal locations of the absorption coefficient. The left panel shows a zoom in the absorption. (b) $\mathrm{Im}[\rho_{12}]$ with $\Omega_p/2\pi = 7.5$ kHz (black solid line), 30 kHz (blue dashed line), and 75 kHz (red dot-dashed line). Here, $\gamma_2/2\pi = 7.5$ kHz and the other parameters are the same as (a). (c) The visibility as a function of γ_2 with $\Omega_m/2\pi = 50$ kHz (black solid line), 0.2 MHz (blue dashed line), and 1 MHz (red dot-dashed line). (d) The visibility as a function of Ω_p with $\gamma_2/2\pi = 7.5$ kHz, $\Omega_m/2\pi = 50$ kHz (black solid line), 0.2 MHz (blue dashed line), and 1 MHz (red dot-dashed line).

B. EIA regime

In the far-detuned case $|\delta_3| \sim |\delta_2| \gg \delta, \Omega_c$, and γ_2, the state $|2\rangle$ can be adiabatically eliminated, leading to the EIA scheme [Fig. 1(c)]. This yields an effective three-level Hamiltonian [14],

$$H_{\mathrm{eff}} = (\delta + \delta_{\mathrm{ac}})|3\rangle\langle 3| + \delta_4|4\rangle\langle 4| + \frac{\Omega_{\mathrm{eff}}}{2}|1\rangle\langle 3| + \frac{\Omega_m}{2}|3\rangle\langle 4| + \mathrm{H.c.}, \quad (11)$$

where $\Omega_{\mathrm{eff}} = \Omega_c\Omega_p/2\delta_3$ is an effective Rabi frequency, and $\delta_{\mathrm{ac}} = (\Omega_p^2 + \Omega_c^2)/4\delta_3$ is the ac Stark shift. When $\Omega_{\mathrm{eff}} \ll \Omega_m$,

an analytic solution of the two-photon coherence is obtained,

$$\rho_{13} = i\frac{\Gamma_4}{\Omega_m^2 + \Gamma_4(\Gamma_3 - 2i\delta_{\rm ac})}\Omega_{\rm eff}. \tag{12}$$

The maximal absorption occurs when the real part of the denominator vanishes at

$$\delta_\pm = -\tfrac{1}{2}[\delta_{\rm ac} + \delta_m \pm A(\delta_m)], \tag{13}$$

with $A(\delta_m) = \sqrt{\Omega_m^2 + \gamma_3\gamma_4 + (\delta_{\rm ac} - \delta_m)^2}$. When $\delta_m = 0$, we obtain ρ_{13} at $\delta_\pm$,

$$\rho_{13}^{(\pm)} = \frac{iA(0) \pm (\gamma_4 + i\delta_{\rm ac})}{A(0)(\gamma_4 + \gamma_3) \pm \delta_{\rm ac}(\gamma_3 - \gamma_4)}\Omega_{\rm eff}, \tag{14}$$

which shows that the absorption is asymmetric when $\delta_{\rm ac} \neq 0$. Note that coherence becomes a pure real value, $\rho_{13} = \frac{2\delta_4\Omega_{\rm eff}}{\Omega_m^2 - 4\delta_4(\delta_3+\delta_{\rm ac})}$, when neglecting Rydberg state decay $\gamma_3 = \gamma_4 = 0$.

When $\delta_m = 0$ and $\Omega_m \gg \delta_{\rm ac}$, the coherence is approximately given by

$$\rho_{13} \approx -\frac{\Omega_{\rm eff}}{2}\left[\frac{1}{2\delta + \Omega_m + i\gamma_3} + \frac{1}{2\delta - \Omega_m + i\gamma_3}\right]. \tag{15}$$

It contains two equal-width (width γ_3) Lorentzian peaks shifted by $\pm\Omega_m/2$ from the two-photon resonance frequency. The two absorption peaks of the coherence can be used to sense MW fields [36] whose splitting is equal to Ω_m, as has been demonstrated in a recent experiment [14].

When $\delta = \pm\Omega_m/2$, the saturation parameter is obtained,

$$s = \left(\frac{\Omega_{\rm eff}}{2\gamma_3}\right)^2 = \left(\frac{\Omega_c\Omega_p}{4\gamma_3\delta_3}\right)^2. \tag{16}$$

Compared to the EIT regime, the saturation parameter in the EIA regime will rely on the Rydberg state decay rate. For given Rydberg states, strong absorption can be obtained by using large Ω_c and Ω_p, and small δ_3. Note that the latter means that γ_2 needs to be small, as the adiabatic elimination requires $\delta_3 \gg \gamma_2$.

In Fig. 4, we show the absorption spectrum obtained by numerically solving the original master equation (2). The absorption peaks agree with the analytical result, especially when γ_2 is small. Though $\delta_\pm$ is independent of γ_2, the width of the absorption peak increases with increasing γ_2. $\delta_\pm$ is not symmetric and depends non-negligibly on Rabi frequencies of the probe and MW fields. In Fig. 4(b), the location of the peaks shifts to the positive δ with increasing Ω_p, due to the Stark shift, though the distance between the peaks is unchanged. In Fig. 4(c), one can clearly observe when the MW field is weak, $\Omega_m \leqslant \delta_{\rm ac}$, and the two absorption peaks are asymmetric, as shown in Eq. (14). When Ω_m is strong enough, $\Omega_m \gg \delta_{\rm ac}$, the symmetry of the two absorptions is nearly restored, which is consistent with Eq. (15). One important figure of merit is the contrast between the height of the peaks and the lowest value between the two peaks. The resulting visibility is plotted in Figs. 4(d) and 4(e). Similar to the EIT case, the visibility increases with increasing Ω_m (decreasing γ_2) with fixed γ_2 (Ω_m). Moreover, when $\Omega_p > \Omega_c$, the visibility decreases dramatically with increasing Ω_p.

In Figs. 5(a) and 5(b), we compare the absorption spectrum when $\gamma_2 = 2\pi \times 6$ MHz and $\gamma_2 = 2\pi \times 7.5$ kHz,

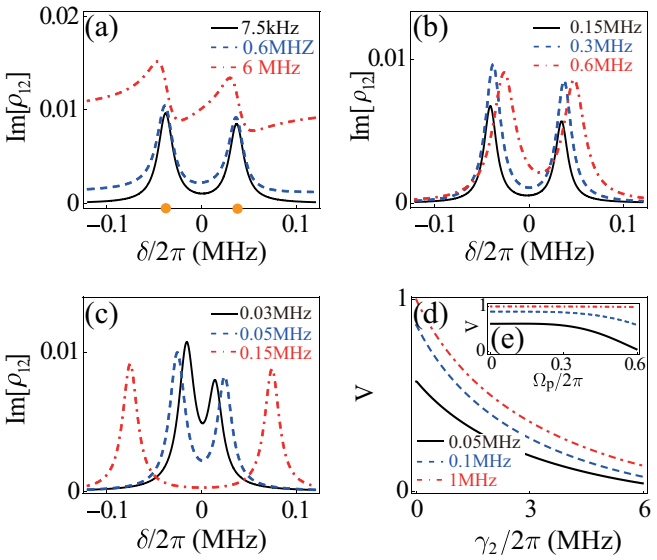

FIG. 4. (a) The absorption spectrum with $\gamma_2/2\pi = 7.5$ kHz (black solid line), 0.6 MHz (blue dashed line), and 6 MHz (red dot-dashed line) in the far-detuning case ($\delta_3/2\pi = 6$MHz). The other parameters are $\gamma_3/2\pi = \gamma_4/2\pi = 15$ kHz, $\Omega_p/2\pi = 0.3$ MHz, $\Omega_c/2\pi = 0.45$ MHz, $\Omega_m = 5\gamma_3$, and $\delta_{\rm m} = 0$. The filled circles in the axis give the locations of the maximal absorption. (b) The absorption spectrum with $\Omega_p/2\pi = 0.15$ MHz (black solid line), 0.3 MHz (blue dashed line), and 0.6 MHz (red dot-dashed line). Here, $\gamma_2/2\pi = 7.5$ kHz and the other parameters are the same as (a). (c) The absorption spectrum with $\Omega_m/2\pi = 0.03$ MHz (black solid line), 0.05 MHz (blue dashed line), and 0.15 MHz (red dot-dashed line). (d) Visibility as a function of γ_2 with $\Omega_m/2\pi = 0.05$ MHz (black solid line), 0.1 MHz (blue dashed line), and 1 MHz (red dot-dashed line). (e) Visibility as a function of Ω_p with $\Omega_m/2\pi = 0.05$ MHz (black solid line), 0.1 MHz (blue dashed line), and 1 MHz (red dot-dashed line). The other parameters in (c)–(e) are the same as (b).

respectively. The resulting absorption spectrum is asymmetric in Fig. 5(a), as the large detuning condition is not fully met. The absorption peaks sit on a non-negligible background such that the contrast is low. To meet the EIA condition, even larger δ_3 is needed, which would lead to weaker absorption [14]. On the contrary, we can balance the large detuning condition and high saturation to achieve high contrast when γ_2 is small. As shown in Fig. 5(b), the absorption spectrum becomes symmetric and the distance between the EIA peaks is Ω_m. The above results show that the EIA spectrum of Sr triplet states is robust. The high visibility might be beneficial to sensing weak MW fields.

C. Finite-temperature effects

In this section, we briefly discuss the Doppler effect due to finite temperature $T > 0$ of the atomic gas. We will show that the main conclusions are still valid, even though the (absorption or transmission) signal becomes weaker. We assume that the probe and control light counterpropagate, where the Doppler effect is integrated into the detuning through $\delta_p' = \delta_2 + (2\pi/\lambda_p)v$, $\delta_c' = \delta_3 - (2\pi/\lambda_c)v$, with v the atomic velocity [37,38]. Doppler shifts of the MW field are small and can be ignored. We average the steady-state solution of ρ_{12} over

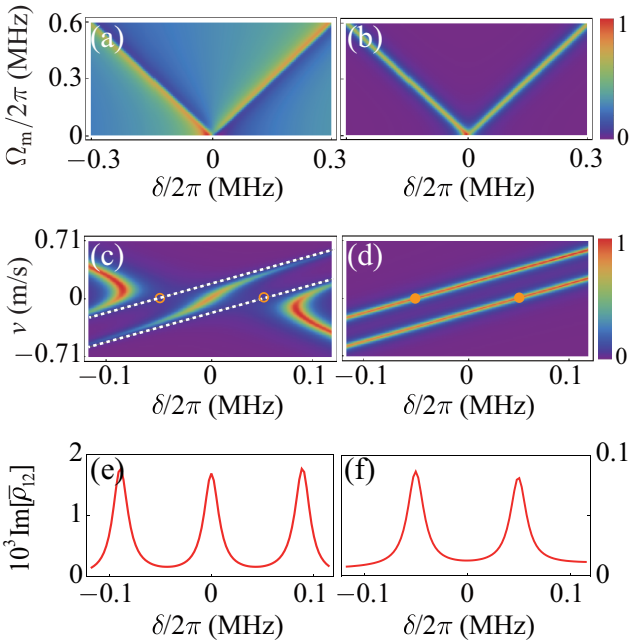

FIG. 5. (a), (b) The absorption spectrum with (a) $\gamma_2 = 2\pi \times 6$ MHz and (b) $\gamma_2 = 2\pi \times 7.5$ kHz. The other parameters are $\gamma_3 = \gamma_4 = 2\pi \times 15$ kHz, $\Omega_\mathrm{p} = 2\pi \times 0.3$ MHz, $\Omega_\mathrm{c} = 0.45$ MHz, $\delta_\mathrm{m} = 0$, $\delta_3 = 2\pi \times 6$ MHz. (c), (d) Absorption (normalized) vs atom velocity and detuning δ with $T = 300$ K, $\gamma_2 = 2\pi \times 7.5$ kHz, $\gamma_3 = \gamma_4 = 2\pi \times 15$ kHz, and $\Omega_m = 2\pi \times 0.1$ MHz. The dashed lines in (c) show that the absorption dips are shifted. The open (filled) circles indicate the absorption dip (peak) locations when the atoms do not move, i.e., $v = 0$. The other parameters are (c) EIT regime: $\delta_3 = 0$, $\Omega_p = 2\pi \times 15$ kHz, $\Omega_c = 2\pi \times 150$ kHz, (d) EIA regime: $\delta_3 = 2\pi \times 6$ MHz, $\Omega_p = 2\pi \times 0.3$ MHz, $\Omega_c = 2\pi \times 0.45$ MHz. (e), (f) The corresponding Doppler averaged absorption spectrum in the (e) EIT and (f) EIA regime.

the atomic velocity distribution that is found in a vapor cell at temperature T with $\bar{\rho}_{12} = \int dv f(v)\rho_{12}(\delta_p', \delta_c')$. Here, $f(v) = 1/(\sqrt{\pi}u)\exp[-(v/u)^2]$ is the Maxwell-Boltzmann velocity distribution [37,39] with $u = \sqrt{2k_BT/m}$ the root-mean-square atom velocity at temperature T and m the mass of the atom.

The absorption spectrum of the atoms with different velocities and the Doppler averaged absorption spectrum in the EIT regime and EIA regime are shown in Figs. 5(c)–5(f). In Fig. 5(c), the absorption peak in the center $\delta = 0$ is shifted by $2\pi/\lambda_p v$ and represents the one-photon resonance signal of the probe beam. The two absorption minima around $\delta = \pm\Omega_m/2$ (the open circles, at zero temperature) are shifted by the Doppler shift $(2\pi/\lambda_p - 2\pi/\lambda_c)v$ of the two-photon resonance [the dashed lines in Fig. 5(c)] due to the wavelength difference between the probe and control fields. As a result, the contribution from each velocity class strongly reduces the visibility of the probe absorption spectrum compared to the Doppler-free case, as depicted in Figs. 5(e). However, in the EIA regime, as shown in Fig. 5(d), the two absorption peaks are shifted by the Doppler shift of the two-photon resonance to be $(2\pi/\lambda_p - 2\pi/\lambda_c)v$ and the one-photon Doppler shift is absent because of the large one-photon detuning. The above analysis shows that the EIA feature persists even in the presence of Doppler effects [Fig. 5(f)].

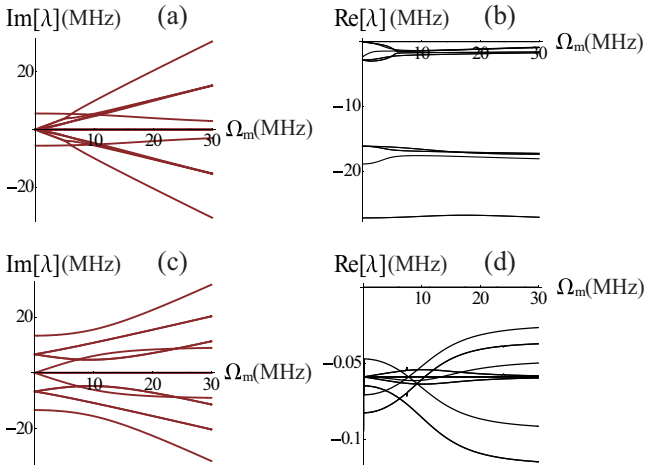

FIG. 6. The imaginary and real parts of the spectrum of the Liouville operator $\mathcal{L}$ when (a), (b) $\gamma_2 = 2\pi \times 6$ MHz and (c), (d) $\gamma_2 = 2\pi \times 7.5$ kHz. The other parameters are $\gamma_3 = \gamma_4 = 2\pi \times 15$ kHz, $\Omega_p = \Omega_c = 2\pi \times 1.5$ MHz, and $\delta_2 = \delta_3 = \delta_m = 0$

IV. RESONANCE FLUORESCENCE

A. Timescales in the EIT and EIA schemes

So far our analysis has been focused on the stationary coherence. When γ_2 is small, one would expect that the system takes a longer time to reach the stationary state. The response time of the system depends on a number of parameters [40–42]. Here we investigate the timescale of the dynamics in the EIT and EIA regimes through analyzing the master equation. We calculate eigenvalues λ_k of the Liouville operator $\mathcal{L}$ [43],

$$\mathcal{L}R_k = \lambda_k R_k, \tag{17}$$

$$L_k\mathcal{L} = \lambda_k L_k, \tag{18}$$

with eigenvalues λ_k, $(k = 1, 2, \dots)$, and left and right eigenvectors L_k and R_k, respectively. The orthogonality and completeness of the eigenvectors are defined in respect to the trace, such that $\mathrm{Tr}\{L_kR_{k'}\} = \delta_{k,k'}$. Eigenvalue $\lambda_1 = 0$ and the corresponding eigenvector give the stationary state of the master equation.

If the MW field and the decay rate are small, $\Omega_m, \gamma_2 \ll \Omega_p, \Omega_c$, the imaginary part of the eigenvalues can be approximately obtained. The first two sets of solutions are $\mathrm{Im}[\lambda] \simeq \{0, \pm\sqrt{\Omega_p^2 + \Omega_c^2}\}$ independent of Ω_m. The other two sets of solutions to $\mathrm{Im}[\lambda]$ are

$$\left\{\pm 9\sqrt{\frac{\gamma_2}{\Omega_c}}\Omega_m, \frac{\pm\sqrt{\Omega_p^2 + \Omega_c^2}}{2} \pm 6\sqrt{\frac{\gamma_2}{\Omega_c}}\Omega_m\right\}. \tag{19}$$

The approximate solutions show that $\mathrm{Im}[\lambda_k]$ that are between 0 and the maximum (minimum) will be linearly changing with Ω_m. In Fig. 6, the numerical spectrum of operator $\mathcal{L}$ as a function of Ω_m for (a), (b) $\gamma_2 = 2\pi \times 6$ MHz and (c), (d)

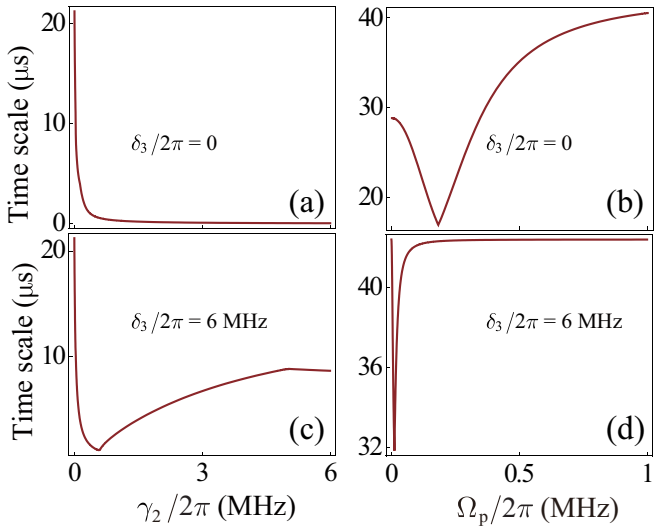

FIG. 7. Timescale in the (a), (b) EIT and (c), (d) EIA regimes. We consider (a) $\Omega_p = 2\pi \times 7.5$ kHz and (b) $\gamma_2 = 2\pi \times 7.5$ kHz with $\gamma_3 = \gamma_4 = 2\pi \times 15$ kHz, $\delta_2 = \delta_3 = \delta_m = 0$, $\Omega_c = 2\pi \times 75$ kHz, and $\Omega_m = 2\pi \times 0.16$ MHz. In the EIA regime, we consider (c) $\Omega_p = 2\pi \times 0.3$ MHz and (d) $\gamma_2 = 2\pi \times 7.5$ kHz with $\delta_3 = 2\pi \times 6$ MHz. The other parameters are $\gamma_3 = \gamma_4 = 2\pi \times 15$ kHz, $\delta_2 = \delta_m = 0$, $\Omega_c = 2\pi \times 0.45$ MHz, and $\Omega_m = 2\pi \times 0.16$ MHz.

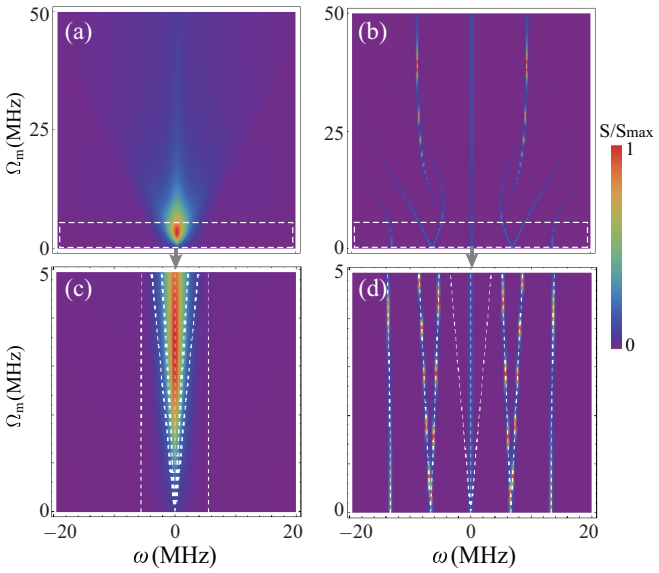

FIG. 8. The spectrum of resonance fluorescence as a function of Ω_m with (a) $\gamma_2 = 2\pi \times 6$ MHz, (b) $\gamma_2 = 2\pi \times 7.5$ kHz. (c), (d) The enlarged region marked by the white box in (a) and (b). The dashed lines indicate imaginary parts of λ_k. The other parameters are the same as Fig. 6.

$\gamma_2 = 2\pi \times 7.5$ kHz are shown. The linear dependence can be seen in the figure when Ω_m is small.

$|\mathrm{Re}[\lambda_k]|$ gives the relaxation rate of the kth mode. The inverse of the real part of the second largest eigenvalue, $1/|\mathrm{Re}[\lambda_2]|$, gives the longest time required for the system to evolve to a stationary state [44]. We plot the longest timescale in the EIT [$\delta_3 = 0$, Figs. 7(a) and 7(b)] and EIA [$\delta_3 = 2\pi \times 6$ MHz, Figs. 7(c) and 7(d)] regimes, respectively. For large γ_2, it takes shorter times to reach the steady state in the EIA than in the EIT regime. When γ_2 is small, the timescale between the EIT and EIA schemes is similar. As shown in Figs. 7(b) and 7(d), the timescale no longer changes monotonously with Ω_p. A sharp dip appears in the timescale due to the degeneracy of $\mathrm{Re}[\lambda_2]$ and $\mathrm{Re}[\lambda_3]$. The above analysis shows that when γ_2 is small, it could take a significant amount of time to reach the steady state. Such slow timescale could be probed, for example, by measuring the time-dependent probe light transmission [41].

B. Spectrum of resonance fluorescence

In the rest of the work, we investigate the spectrum of resonance fluorescence of Sr atoms. We will identify a linear relation between the spectrum and MW field, which could provide an alternative way to measure weak MW fields. The power spectrum is given by the transform of the optical field autocorrelation function [45],

$$S(\omega, t) = \mathrm{Re}\int_0^\infty d\tau e^{-i\omega\tau}\langle\sigma_{21}(t)\sigma_{12}(\tau + t)\rangle. \tag{20}$$

Using quantum regression theorem, the two-time correlation function can be calculated,

$$\langle\sigma_{21}(t)\sigma_{12}(t + \tau)\rangle = \mathrm{Tr}[\sigma_{12}\Lambda(t + \tau, t)], \tag{21}$$

where $\Lambda(t + \tau, t)$ satisfies the evolution equation

$$\partial_\tau \Lambda(t + \tau, t) = \mathcal{L}\Lambda(t + \tau, t), \tag{22}$$

and the initial condition is

$$\Lambda(t, t) = \rho(t)\sigma_{21}. \tag{23}$$

One can find that $\Lambda(t + \tau, t) = e^{\mathcal{L}\tau}\Lambda(t, t)$, so that

$$\begin{aligned} S(\omega, t) &= \mathrm{Re}\int_0^\infty d\tau e^{-i\omega\tau}\mathrm{Tr}[\sigma_{12}\Lambda(t + \tau, t)] \\ &= \mathrm{Re}\left[\frac{1}{i\omega - \mathcal{L}}\sum_k \mathrm{Tr}[\sigma_{12}e^{t\lambda_k}c_k R_k\sigma_{21}]\right], \end{aligned} \tag{24}$$

where $c_k = \mathrm{Tr}[L_k\rho_{in}]$.

When $t \to \infty$, $\lim_{t\to\infty}\Lambda(t, t) = \rho_{ss}\sigma_{21} = \Lambda(0)$. The corresponding stationary spectrum can be obtained,

$$\begin{aligned} S(\omega) &= \mathrm{Re}\int_0^\infty d\tau e^{-i\omega\tau}\mathrm{Tr}[\sigma_{12}\Lambda(\tau)] \\ &= \mathrm{Re}\left[\sum_k \frac{1}{i\omega - \lambda_k}\mathrm{Tr}[\sigma_{12}c_k R_k\sigma_{21}]\right], \end{aligned} \tag{25}$$

which indicates that the spectrum of resonance fluorescence is the sum of the Lorentz profile, centered at the imaginary part of the eigenvalues of $\mathcal{L}$, with width given by the real part of λ_k. The fluorescence spectrum can also be understood by analyzing eigenenergies of the dressed states [46–48].

In the stationary state, the peaks acquires a wider linewidth when γ_2 is large [see Fig. 6(b)]. The wide linewidth will suppress peaks for $\omega \neq 0$ [see Figs. 8(a) and 8(c)]. When γ_2 is smaller than $\Omega_p(c)$, the system is in the so-called strongly driven regime. A well-studied example in this regime is the so-called Mollow triplet of two-level atoms [30]. Multiple

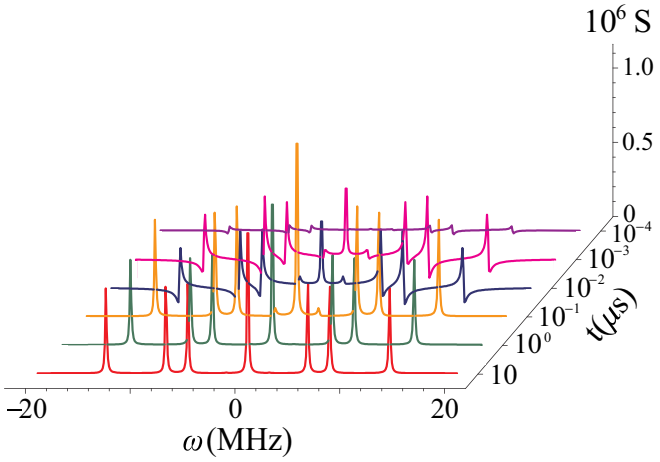

FIG. 9. Time-dependent fluorescence spectrum for $\gamma_2 = 2\pi \times 7.5$ kHz. Other parameters are $\gamma_3 = \gamma_4 = 2\pi \times 15$ kHz, $\Omega_m \approx 2\pi \times 0.48$ MHz, and $\Omega_c = \Omega_p = 2\pi \times 1.5$ MHz.

peaks can be observed in the spectrum of the resonance fluorescence, and the distance between the peaks near the center peak increases linearly with increasing Ω_m for weak MW fields, as shown in Figs. 8(b) and 8(d). These peaks have particularly narrow linewidth, as the real parts of λ_k are small [see Fig. 6(d)]. The linear dependence on Ω_m potentially allows us to identify the MW field Rabi frequency (e.g., when the strength of the MW field drifts slowly with time) by measuring the distance between these two peaks, opening perspectives to develop Rydberg MW electrometry based on Sr atoms.

Finally, we address the time-dependent fluorescence spectrum, shown in Fig. 9. Initially, the heights of the fluorescence peaks are low. These peaks increase with increasing interaction time. The spectrum approaches the stationary distribution when $t > 10\ \mu$s. Here the timescale in the dynamical evolution of the spectrum is largely determined by $1/\gamma_2$, consistent with the analysis of the eigenvalues of the Liouville operator. These timescales are much smaller than the motional dephasing in cold and ultracold atom gases, and hence could be measured in current experiments.

V. CONCLUSION

We have studied the optical responses of the Sr triplet optical transition and showed that a weak MW field can be sensed through using combined EIT and AT splitting, as well as EIA. The significantly small decay rate in the triplet state affects the transparency spectrum in the Rydberg EIT. The stationary transmission, compared with alkali-metal atoms, becomes weaker. Narrow and strong absorption peaks are found neighboring the weakened transparent window, leading to apparent differences between the transparent and absorption strength (Fig. 3). In the EIA regime, the maximal absorption is increased from the background absorption. The distance of the transparent windows (EIT) and the absorption peaks (EIA), given by Ω_m, can be as small as the decay rate γ_2 of the intermediate state. The high contrast in both approaches is beneficial when sensing the MW field with Sr Rydberg states. Moreover, we have examined resonance fluorescence of the lower transition in the four-level system. Mathematically, it is found that the location of the florescence peaks is determined by the imaginary parts of the Liouville operator. We have shown that the distance between neighboring peaks is linearly proportional to the MW field Rabi frequency when $\Omega_m \sim \gamma_2 \ll \Omega_c, \Omega_m$. Such dependence is not visible in the case of alkali-metal atoms because the decay rate in the respective state is large and so one might be able to measure weak MW fields coupled to triplet Rydberg states with Sr atoms. In the EIT-AT and EIA methods, one directly measures the transmission and absorption of the probe light. In resonance fluorescence, photons scattered by the atoms are collected and measured. This method provides an opportunity to sense MW fields when directly measuring the transmission or absorption is not possible, or difficult to achieve.

ACKNOWLEDGMENTS

We are thankful for insightful discussions with Dr. Peng Xu and Prof. Hui Yan. This work was supported by the National Nature Science Foundation of China (Grants No. 12074433, No. 11871472, No. 11874004, No. 11204019, and No. 12174448), National Basic Research Program of China (Grant No. 2016YFA0301903), Science Foundation of Education Department of Jilin Province (Grant No. JJKH20200557KJ), and Nature Science Foundation of Science and Technology Department of Jilin Province (Grant No. 20210101411JC).

[1] C. L. Degen, F. Reinhard, and P. Cappellaro, Quantum sensing, Rev. Mod. Phys. **89**, 035002 (2017).

[2] C. G. Wade, N. Š, N. R. De Melo, J. M. Kondo, C. S. Adams, and K. J. Weatherill, Real-time near-field terahertz imaging with atomic optical fluorescence, Nat. Photon. **11**, 40 (2017).

[3] C. S. Adams, J. D. Pritchard, and J. P. Shaffer, Rydberg atom quantum technologies, J. Phys. B: At. Mol. Opt. Phys. **53**, 012002 (2019).

[4] J. A. Sedlacek, A. Schwettmann, H. Kübler, R. Löw, T. Pfau, and J. P. Shaffer, Microwave electrometry with Rydberg atoms in a vapour cell using bright atomic resonances, Nat. Phys. **8**, 819 (2012).

[5] S. Kumar, H. Fan, H. Kübler, A. J. Jahangiri, and J. P. Shaffer, Rydberg-atom based radio-frequency electrometry using frequency modulation spectroscopy in room temperature vapor cells, Opt. Express **25**, 8625 (2017).

[6] S. Kumar, H. Fan, H. Kübler, J. Sheng, and J. P. Shaffer, Atom-Based Sensing of Weak Radio Frequency Electric Fields Using Homodyne Readout, Sci. Rep. **7**, 42981 (2017).

[7] M. Jing, Y. Hu, J. Ma, H. Zhang, L. Zhang, L. Xiao, and S. Jia, Atomic superheterodyne receiver based on microwave-dressed Rydberg spectroscopy, Nat. Phys. **16**, 911 (2020).

[8] J. A. Gordon, C. L. Holloway, A. Schwarzkopf, D. A. Anderson, S. Miller, N. Thaicharoen, and G. Raithel, Millimeter wave detection via Autler-Townes splitting in rubidium Rydberg atoms, Appl. Phys. Lett. **105**, 024104 (2014).

[9] J. Millen, G. Lochead, and M. P. A. Jones, Two-Electron Excitation of an Interacting Cold Rydberg Gas, Phys. Rev. Lett. **105**, 213004 (2010).

[10] R. Ding, J. D. Whalen, S. K. Kanungo, T. C. Killian, F. B. Dunning, S. Yoshida, and J. Burgdörfer, Spectroscopy of ^{87}Sr triplet Rydberg states, Phys. Rev. A **98**, 042505 (2018).

[11] C. Qiao, C. Z. Tan, F. C. Hu, L. Couturier, I. Nosske, P. Chen, Y. H. Jiang, B. Zhu, and M. Weidemüller, An ultrastable laser system at 689 nm for cooling and trapping of strontium, Appl. Phys. B **125**, 215 (2019).

[12] C. L. Holloway, J. A. Gordon, A. Schwarzkopf, D. A. Anderson, A. M. Stephanie, N. Thaicharoen, and G. Raithel, Sub-wavelength imaging and field mapping via electromagnetically induced transparency and Autler-Townes splitting in Rydberg atoms, Appl. Phys. Lett. **104**, 244102 (2014).

[13] H. Fan, S. Kumar, J. Sedlacek, and H. Kübler, Atom based RF electric field sensing, J. Phys. B: At. Mol. Opt. Phys. **48**, 202001 (2015).

[14] K.-Y. Liao, H.-T. Tu, S.-Z. Yang, C.-J. Chen, X.-H. Liu, J. Liang, X.-D. Zhang, H. Yan, and S.-L. Zhu, Microwave electrometry via electromagnetically induced absorption in cold Rydberg atoms, Phys. Rev. A **101**, 053432 (2020).

[15] A. M. Akulshin, S. Barreiro, and A. Lezama, Electromagnetically induced absorption and transparency due to resonant two-field excitation of quasidegenerate levels in Rb vapor, Phys. Rev. A **57**, 2996 (1998).

[16] F. B. Dunning, T. C. Killian, S. Yoshida, and J. Burgdörfer, Recent advances in Rydberg physics using alkaline-earth atoms, J. Phys. B: At. Mol. Opt. Phys. **49**, 112003 (2016).

[17] I. S. Madjarov, J. P. Covey, A. L. Shaw, J. Choi, A. Kale, A. Cooper, H. Pichler, V. Schkolnik, J. R. Williams, and M. Endres, High-fidelity entanglement and detection of alkaline-earth Rydberg atoms, Nat. Phys. **16**, 857 (2020).

[18] B. J. DeSalvo, J. A. Aman, C. Gaul, T. Pohl, S. Yoshida, J. Burgdörfer, K. R. A. Hazzard, F. B. Dunning, and T. C. Killian, Rydberg-blockade effects in Autler-Townes spectra of ultracold strontium, Phys. Rev. A **93**, 022709 (2016).

[19] C. Qiao, C. Tan, J. Siegl, F. Hu, Z. Niu, Y. Jiang, M. Weidemüller, and B. Zhu, Rydberg blockade in an ultracold strontium gas revealed by two-photon excitation dynamics, Phys. Rev. A **103**, 063313 (2021).

[20] C. Gaul, B. J. DeSalvo, J. A. Aman, F. B. Dunning, T. C. Killian, and T. Pohl, Resonant Rydberg Dressing of Alkaline-Earth Atoms via Electromagnetically Induced Transparency, Phys. Rev. Lett. **116**, 243001 (2016).

[21] F. Camargo, R. Schmidt, J. D. Whalen, R. Ding, G. Woehl, Jr., S. Yoshida, J. Burgdörfer, F. B. Dunning, H. R. Sadeghpour, E. Demler, and T. C. Killian, Creation of Rydberg Polarons in a Bose Gas, Phys. Rev. Lett. **120**, 083401 (2018).

[22] P. Kómár, E. M. Kessler, M. Bishof, L. Jiang, A. S. Sørensen, J. Ye, and M. D. Lukin, A quantum network of clocks, Nat. Phys. **10**, 582 (2014).

[23] L. I. R. Gil, R. Mukherjee, E. M. Bridge, M. P. A. Jones, and T. Pohl, Spin Squeezing in a Rydberg Lattice Clock, Phys. Rev. Lett. **112**, 103601 (2014).

[24] F. Robicheaux, Calculations of long range interactions for 87Sr Rydberg states, J. Phys. B: At. Mol. Opt. Phys. **52**, 244001 (2019).

[25] C. Tan, X. Lin, Y. Zhou, Y. Jiang, M. Weidemüller, and B. Zhu, Dynamics of position-disordered Ising spins with a soft-core potential, Phys. Rev. B **105**, 104204 (2022).

[26] E. M. Kessler, P. Kómár, M. Bishof, L. Jiang, A. S. Sørensen, J. Ye, and M. D. Lukin, Heisenberg-Limited Atom Clocks Based on Entangled Qubits, Phys. Rev. Lett. **112**, 190403 (2014).

[27] R. Kaubruegger, P. Silvi, C. Kokail, R. van Bijnen, A. Maria Rey, J. Ye, A. M. Kaufman, and P. Zoller, Variational Spin-Squeezing Algorithms on Programmable Quantum Sensors, Phys. Rev. Lett. **123**, 260505 (2019).

[28] L. Couturier, I. Nosske, F. Hu, C. Tan, C. Qiao, Y. H. Jiang, P. Chen, and M. Weidemüller, Measurement of the strontium triplet Rydberg series by depletion spectroscopy of ultracold atoms, Phys. Rev. A **99**, 022503 (2019).

[29] F. Hu, C. Tan, Y. Jiang, M. Weidemüller, and B. Zhu, Observation of photon recoil effects in single-beam absorption spectroscopy with an ultracold strontium gas, Chinese Phys. B **31** 016702 (2022).

[30] B. R. Mollow, Power spectrum of light scattered by two-level systems, Phys. Rev. **188**, 1969 (1969).

[31] M. O. Scully and M. Suhail Zubairy, *Quantum Optics*, 1st ed. (Cambridge University Press, Cambridge, 1997), pp. 291–306.

[32] S. Kunze, R. Hohmann, H. J. Kluge, J. Lantzsch, L. Monz, J. Stenner, K. Stratmann, K. Wendt, and K. Zimmer, Lifetime measurements of highly excited Rydberg states of strontium I, Z. Phys. D: At., Mol. Clusters **27**, 111 (1993).

[33] R. Sadighi-Bonabi and T. Naseri, Theoretical investigation of electromagnetically induced phase grating in RF-driven cascade-type atomic systems, Appl. Opt. **54**, 3484 (2015).

[34] M. Fleischhauer, A. Imamoglu, and J. P. Marangos, Electromagnetically induced transparency: Optics in coherent media, Rev. Mod. Phys. **77**, 633 (2005).

[35] Y. Gao, Y. Ren, D. Yu, and J. Qian, Switchable dynamic Rydberg-dressed excitation via a cascaded double electromagnetically induced transparency, Phys. Rev. A **100**, 033823 (2019).

[36] A. Urvoy, C. Carr, R. Ritter, C. S. Adams, K. J. Weatherill, and R. Löw, Optical coherences and wavelength mismatch in ladder systems, J. Phys. B: At. Mol. Opt. Phys. **46**, 245001 (2013).

[37] C. L. Holloway, M. T. Simons, J. A. Gordon, A. Dienstfrey, D. A. Anderson, and G. Raithel, Electric field metrology for SI traceability: Systematic measurement uncertainties in electromagnetically induced transparency in atomic vapor, J. Appl. Phys. **121**, 233106 (2017).

[38] H. Min Kwak, T. Jeong, Y. Seok Lee, and H. Seb Moon, Microwave-induced three-photon coherence of Rydberg atomic states, Opt. Commun. **380**, 168 (2016).

[39] Z. Bai, C. S. Adams, G. Huang, and W. Li, Self-Induced Transparency in Warm and Strongly Interacting Rydberg Gases, Phys. Rev. Lett. **125**, 263605 (2020).

[40] K. Macieszczak, Y. Zhou, S. Hofferberth, J. P. Garrahan, W. Li, and I. Lesanovsky, Metastable decoherence-free subspaces and electromagnetically induced transparency in interacting many-body systems, Phys. Rev. A **96**, 043860 (2017).

[41] Q. Zhang, Z. Bai, and G. Huang, Fast-responding property of electromagnetically induced transparency

in Rydberg atoms, Phys. Rev. A **97**, 043821 (2018).

[42] Y.-W. Guo, S.-L. Xu, J.-R. He, P. Deng, M. R. Belić, and Y. Zhao, Transient optical response of cold Rydberg atoms with electromagnetically induced transparency, Phys. Rev. A **101**, 023806 (2020).

[43] M. Bienert, W. Merkel, and G. Morigi, Resonance fluorescence of a trapped three-level atom, Phys. Rev. A **69**, 013405 (2004).

[44] K. Macieszczak, M. Guţă, I. Lesanovsky, and J. P. Garrahan, Towards a Theory of Metastability in Open Quantum Dynamics, Phys. Rev. Lett. **116**, 240404 (2016).

[45] D. Adam Steck, Quantum and atom optics; http://steck.us/teaching (rev. 0.12.2).

[46] C.-L. Wang, Z.-H. Kang, S.-C. Tian, Y. Jiang, and J.-Y. Gao, Effect of spontaneously generated coherence on absorption in a V-type system: Investigation in dressed states, Phys. Rev. A **79**, 043810 (2009).

[47] D. Wang and Y. Zheng, Quantum interference in a four-level system of a ^{87}Rb atom: Effects of spontaneously generated coherence, Phys. Rev. A **83**, 013810 (2011).

[48] S.-C. Tian, C.-L. Wang, C.-Z. Tong, L.-J. Wang, H.-H. Wang, X.-B. Yang, Z.-H. Kang, and J.-Y. Gao, Observation of the fluorescence spectrum for a driven cascade model system in atomic beam. Opt. Express **20**, 23559 (2012).